S1. Meteorological forcing downscaling procedures

To smooth the coarse forcing fields and remove artifacts from their native grids, meteorological variables at each model pixel are interpolated from the four nearest native grid cells for NLDAS2 (i.e., Girotto et al., 2014) for MERRA2 and ERA5 (i.e., Fang et al., 2022). Elevation values corresponding to these smoothed forcings are similarly interpolated from the raw forcing product gridded elevation datasets. These smoothed fields and elevations are referred to as the 'interpolated forcings' and 'interpolated elevation', respectively.

The downscaling procedure adjusts interpolated forcings via topographic corrections. Specifically, elevation lapse rates of 6.5 and 4.1°K/km were used for air temperature and dew point temperature, respectively. Atmospheric pressure is downscaled by combining the ideal gas and hydrostatic laws (Cosgrove et al., 2003). Specific humidity follows the method of Liston and Elder (2006). Atmospheric emissivity is calculated based on air temperature, vapor pressure, and three elevation dependent empirical coefficients (Liston and Elder, 2006). Incoming longwave (LW) fluxes are derived from the sum of the downwelling atmospheric LW flux and the LW flux from surrounding terrain (Müller and Scherer, 2005). The downscaling of incoming shortwave (SW) radiation involves: (1) separating the total incoming shortwave radiation into direct and diffuse components (Allen et al., 2006), (2) adjusting these components by elevation corrections (Dubayah and Van Katwijk, 1992), (3) applying topographic corrections based on slope, aspect, shade, and sky view factor (SVF) (Müller and Scherer, 2005), and (4) combining the direct and diffuse components to calculate total incoming shortwave radiation.

S2. Meteorological forcing bias correction and perturbations

The ensemble Bayesian framework considers the key sources of prior uncertainty and error including model parameters (i.e., snow albedo) and meteorological inputs. The bias correction and uncertainty models used in this study are the same as the models applied in generating SWE reanalysis datasets over the WUS (Fang et al., 2022), High Mountain Asia (Liu et al., 2021), and Andes (Cortés and Margulis, 2017). The downscaled prior forcings are bias-corrected and perturbed as:

$$PPT_{i,j} = b_{i,j} \times PPT_i \qquad \text{Eq. S1}$$
$$T_{a,i,j} = T_{a,i} + \varepsilon_{a,i,j} \qquad \text{Eq. S2}$$
$$T_{d,i,j} = T_{d,j} + \varepsilon_{d,i,j} \qquad \text{Eq. S3}$$
$$SW_{i,j} = SW_i \times (1 - \gamma_{i,j}) \qquad \text{Eq. S4}$$

where PPT, T_a, T_d, and SW represent the precipitation, air temperature, dew point temperature, and shortwave radiation, respectively. The subscript i represents the meteorological forcing dataset while j represents the perturbed forcing realization within the ensemble. The random variable b represents a lognormally distributed multiplicative precipitation perturbation. The

random variable ε represents normally distributed additive error perturbations of air temperature and dew point temperature. The random variable γ represents normally distributed multiplicative error perturbations of shortwave radiation and varies with solar index (SI).

The moments of the precipitation parameter b distribution are estimated based on the same methodology described in Fang et al. (2022) from a sub-sample of 10 representative tiles across the WUS spanning a range of physiography and climatology (Fig. S1). The precipitation uncertainty is quantified by running the snow reanalysis framework using a uniform distribution for the parameter b~U(0.1,5) at the 10 tiles. After assimilating fSCA measurements using the PBS approach, a log-normal distribution is fitted to the posterior b values from all pixels and replicates in those 10 tiles. The derivation of uncertainty models for air temperature, dew point temperature, and shortwave radiation followed Girotto et al. (2014) by comparing downscaled forcings to in situ Snow Telemetry network (SNOTEL) and Soil Climate Analysis Network (SCAN) measurements across the WUS. Locations of in situ sites are highlighted in Fig. S1. The differences between downscaled temperature and in situ data are fitted with a normal distribution. The in situ solar radiation measurements and downscaled solar radiation are used to the normal distribution of γ whose mean and standard deviation are polynomial functions of solar index (SI). The distribution of uncertainty parameters for different datasets are summarized in Table S1. Note that the bias-correction is a prior correction applied to the WUS, and the WUS shares the same distribution of uncertainty parameters. Snowfall is computed by downscaled and bias-corrected air temperature and precipitation using a rain-snow threshold of 275.15 K on an hourly basis. When air temperature is below the threshold, precipitation is considered as snowfall.
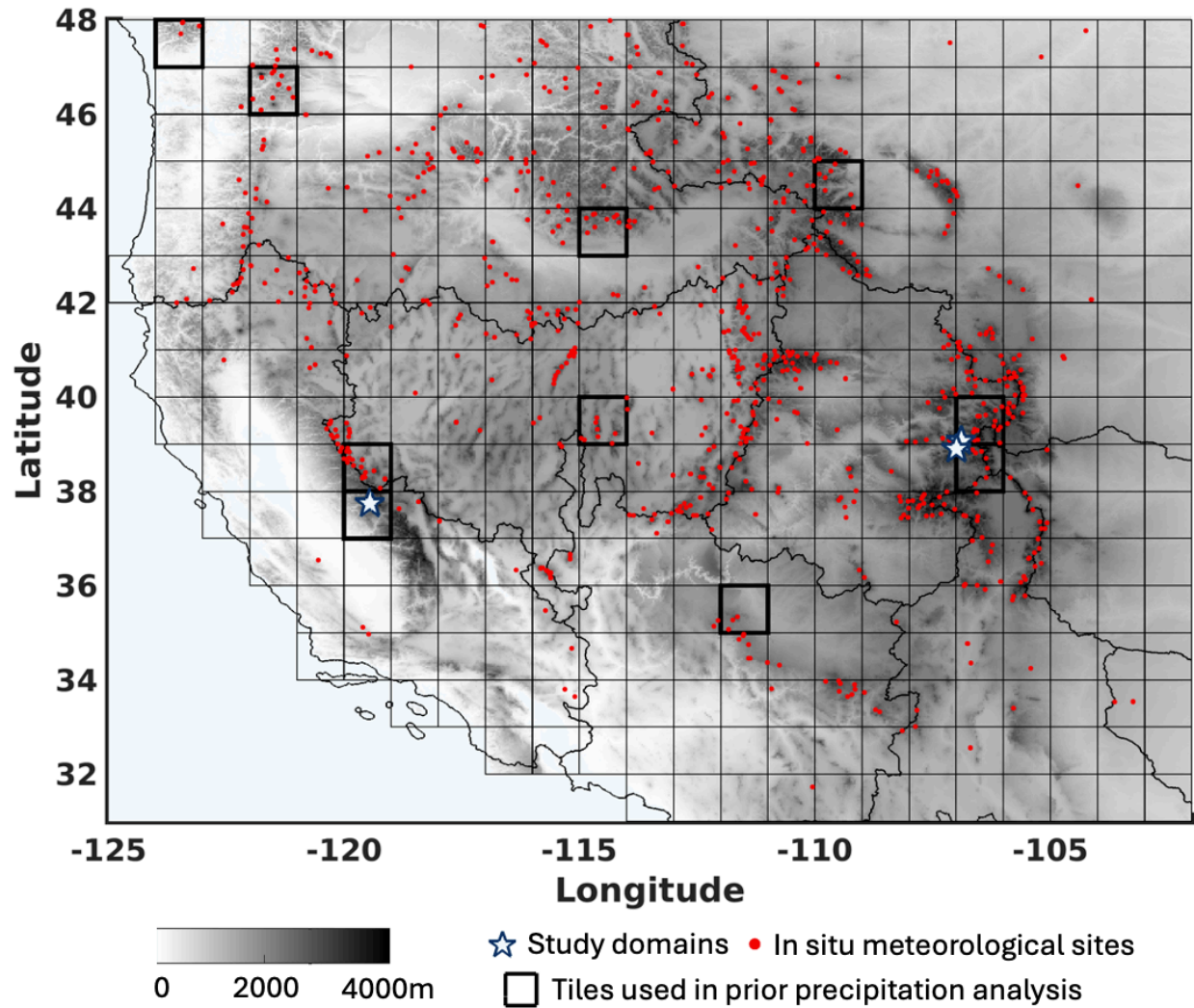
Figure S1. Map of elevation over the WUS HUC2 basins with snow reanalysis tiles ($1^o \times 1^o$ squares). The tiles highlighted with bold black boxes are used for prior precipitation uncertainty analysis. The SNOTEL/SCAN measurements of air temperature, dew point temperature, and shortwave radiation are highlighted with the red dots. The study domains are highlighted with the white stars.

Table S1. Uncertainty model parameters and distributions for ERA5, MERRA2, and NLDAS2.

		ERA5		
b (PPT)	lognormal	Mean	CV	
		1.37	0.88	
ε(T$_a$)	normal	Mean	CV	
		0.53 K	1.34 K	
ε(T$_d$)	normal	Mean	CV	
		-0.61 K	1.24 K	
γ(SW)	normal	Mean	Std. Dev.	Solar Index (SI)
		0.3321	0.32	<0.5
		$3.14SI^3 - 7.17SI^2 + 4.81SI - 0.68$	$-0.24SI + 0.44$	0.5 to 1
		0.1093	0.21	>1
		MERRA2		
b (PPT)	lognormal	Mean	CV	
		1.80	0.69	
ε(T$_a$)	normal	Mean	CV	
		0.85 K	1.39 K	
ε(T$_d$)	normal	Mean	CV	
		-1.37 K	1.20 K	
γ(SW)	normal	Mean	Std. Dev.	Solar Index (SI)
		0.2548	0.39	<0.5
		$3.66SI^3 - 1.88SI^2 + 1.39SI - 0.05$	$-0.39SI + 0.58$	0.5 to 1
		0	0.19	>1
		NLDAS2		
b (PPT)	lognormal	Mean	CV	
		1.88	0.9	
ε(T$_a$)	normal	Mean	CV	
		-0.06 K	1.46 K	
ε(T$_d$)	normal	Mean	CV	
		-0.29 K	1.25 K	
γ(SW)	normal	Mean	Std. Dev.	Solar Index (SI)
		0.2902	0.45	<0.5
		$3.52SI^3 - 8.21SI^2 + 5.56SI - 0.88$	$-0.60SI + 0.75$	0.5 to 1
		0	0.15	>1

S3. Generating ASO-based SWE for Evaluation

The ASO SWE and ASO-based SWE refer to two different SWE products. ASO SWE is a data product generated by combining ASO snow depth observations with snow density estimates derived from the iSnobal energy-balance model (Marks et al., 1999; Painter et al., 2016). In contrast, the ASO-based SWE in this study is computed by combining ASO snow depth observations with average snow density estimates obtained from the SSiB3-SAST model (Sun and Xue, 2001). These snow density estimates are generated from ensemble simulations driven by different meteorological forcing datasets (i.e., ERA5, MERRA2, and NLDAS2). For each ASO measurement day, the ASO-based SWE is calculated using the corresponding model-derived snow density for that day. For the prior analysis, the snow density is taken from the prior model simulations, while for the posterior analysis, it is taken from the reanalysis after assimilation. Since SSiB3-SAST is used as a forward model to generate SWE estimates that are subsequently updated through ASO snow depth assimilation, the ASO-based SWE allows us to evaluate model performance while minimizing the influence of model-based snow density uncertainty. In Fig. S2, ASO SWE is shown as the product of ASO snow depth and ASO snow density, while the ASO-based SWE is computed by multiplying ASO snow depth by the average model derived snow density. The ASO snow density is back-calculated by dividing the ASO SWE product by the ASO snow depth.
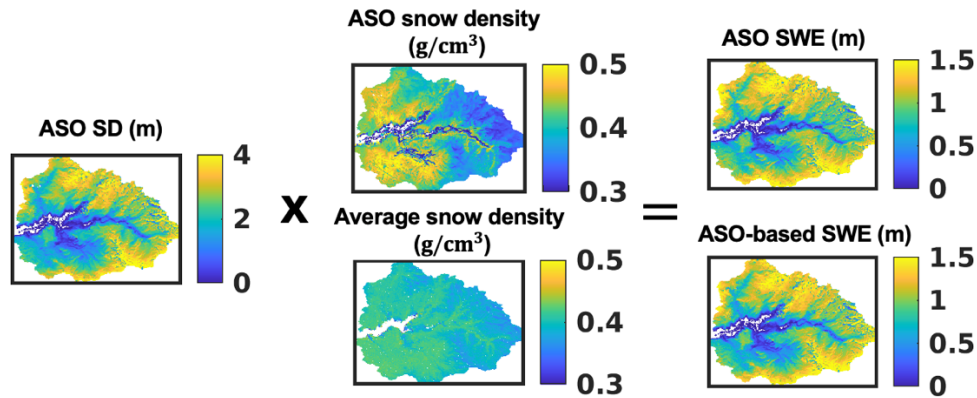
Figure S2. Illustration of ASO SWE and ASO-based SWE derivation. ASO SWE is a product of ASO snow depth and iSnobal modeled snow density (Painter et al., 2016), with snow density here back-calculated as ASO SWE divided by ASO SD. ASO-based SWE is computed using ASO SD and average snow density from the SSiB3-SAST model driven by multiple meteorological forcings.

Building on the ASO-based SWE derivation approach, we generate two versions of ASO-based SWE to enable direct comparison with both prior model simulations and posterior reanalysis outputs. In both cases, ASO-based SWE is calculated by combining ASO snow depth with an average snow density field, either from the model (prior) or from the reanalysis (posterior). This approach provides a consistent basis for SWE comparison that reduces the influence of snow density uncertainty.

Figure S3 shows the average prior snow density at ASO measurement times for Merced, Aspen, and Gunnison-East, derived from SSiB3-SAST simulations forced by ERA5, MERRA2, and NLDAS2. Despite differences in the forcing datasets, the modeled snow densities show limited variation, and their basin-average values are generally consistent. For reference, the ASO snow density, computed by dividing ASO SWE by ASO SD is also shown. The value is only available in regions where ASO snow depth is greater than zero. During snowmelt periods, the ASO-derived snow density tends to be higher than the average modeled density across all domains.
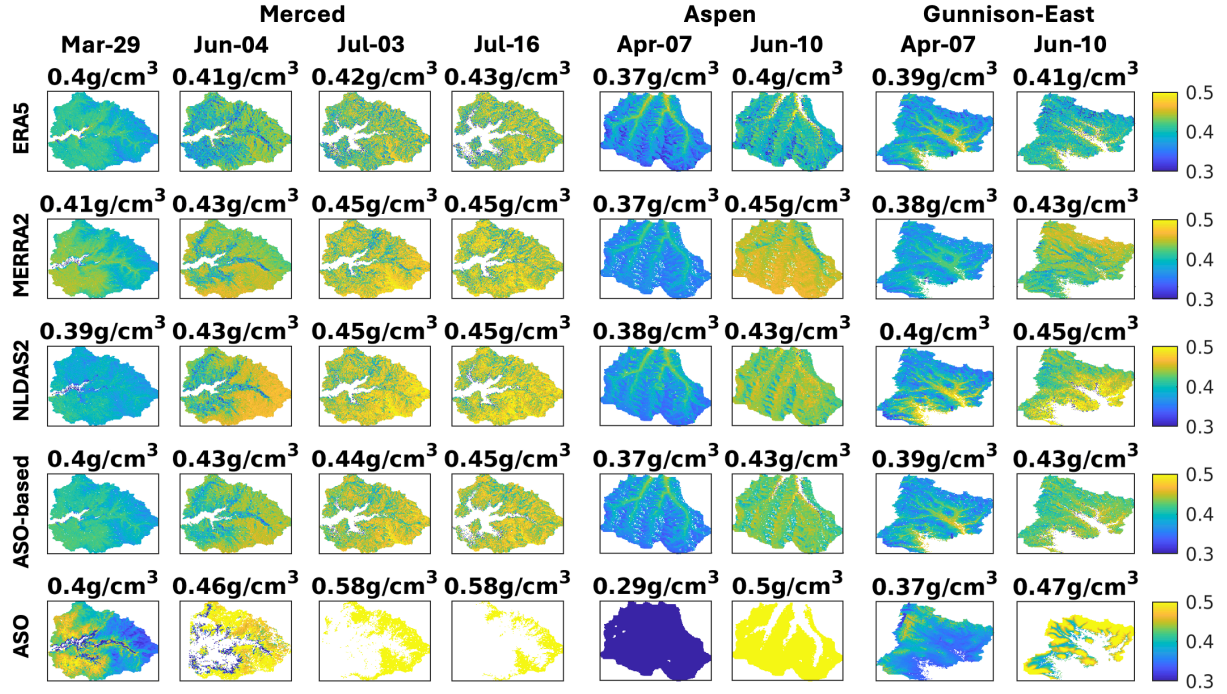
Figure S3. Prior snow density (g/cm^3) at ASO measurement times for Merced, Aspen, and Gunnison-East, derived from SSiB3-SAST simulations forced by ERA5, MERRA2, and NLDAS2. The average modeled snow density is computed by averaging estimates from the three forcing datasets. ASO snow density is also shown, calculated by dividing ASO SWE by ASO snow depth, and is only available in areas where snow depth is greater than zero. Basin-average snow density values are labeled for each map.

We apply the same ASO-based SWE derivation method using the average posterior snow density field (Fig. S4). Note that the posterior snow density fields are similar to the prior estimates in both spatial pattern and magnitude. Therefore, the ASO-based SWE used for prior and posterior comparisons are largely consistent, suggesting that the assimilation process primarily adjusts snow depth while maintaining the modeled snow density.
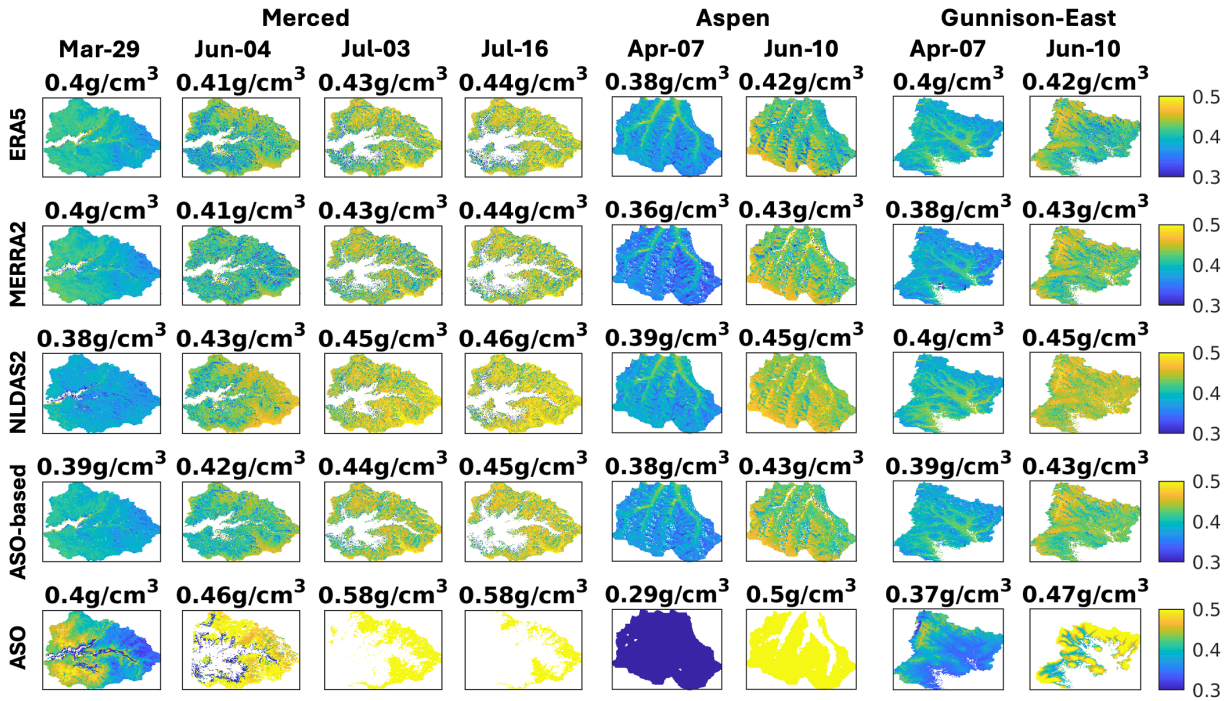
Figure S4. Same as Fig. S3, but for posterior snow density.

Reference:

Allen, R. G., Trezza, R., and Tasumi, M.: Analytical integrated functions for daily solar radiation on slopes, Agric. For. Meteorol., 139, 55–73, https://doi.org/10.1016/j.agrformet.2006.05.012, 2006.

Cortés, G. and Margulis, S.: Impacts of El Niño and La Niña on interannual snow accumulation in the Andes: Results from a high-resolution 31 year reanalysis: El Niño Effects on Andes Snow, Geophys. Res. Lett., 44, 6859–6867, https://doi.org/10.1002/2017GL073826, 2017.

Cosgrove, B. A., Lohmann, D., Mitchell, K. E., Houser, P. R., Wood, E. F., Schaake, J. C., Robock, A., Sheffield, J., Duan, Q., Luo, L., Higgins, R. W., Pinker, R. T., and Tarpley, J. D.: Land surface model spin-up behavior in the North American Land Data Assimilation System (NLDAS), J. Geophys. Res. Atmospheres, 108, https://doi.org/10.1029/2002jd003316, 2003.

Dubayah, R. and Van Katwijk, V.: The topographic distribution of annual incoming solar radiation in the Rio Grande River Basin, Geophys. Res. Lett., 19, 2231–2234, https://doi.org/10.1029/92gl02284, 1992.

Fang, Y., Liu, Y., and Margulis, S. A.: A western United States snow reanalysis dataset over the Landsat era from water years 1985 to 2021, Sci. Data, 9, 677, https://doi.org/10.1038/s41597-022-01768-7, 2022.

Girotto, M., Margulis, S. A., and Durand, M.: Probabilistic SWE reanalysis as a generalization of deterministic SWE reconstruction techniques, Hydrol. Process., 28, 3875–3895, https://doi.org/10.1002/hyp.9887, 2014.

Liston, G. E. and Elder, K.: A Meteorological Distribution System for High-Resolution Terrestrial Modeling (MicroMet), J. Hydrometeorol., 7, 217–234, https://doi.org/10.1175/jhm486.1, 2006.

Liu, Y., Fang, Y., and Margulis, S. A.: Spatiotemporal distribution of seasonal snow water equivalent in High-Mountain Asia from an 18-year Landsat-MODIS era snow reanalysis dataset, Snow/Seasonal Snow, https://doi.org/10.5194/tc-2021-139, 2021.

Müller, M. D. and Scherer, D.: A Grid- and Subgrid-Scale Radiation Parameterization of Topographic Effects for Mesoscale Weather Forecast Models, Mon. Weather Rev., 133, 1431–1442, https://doi.org/10.1175/mwr2927.1, 2005.

Painter, T. H., Berisford, D. F., Boardman, J. W., Bormann, K. J., Deems, J. S., Gehrke, F., Hedrick, A., Joyce, M., Laidlaw, R., Marks, D., Mattmann, C., McGurk, B., Ramirez, P., Richardson, M., Skiles, S. M., Seidel, F. C., and Winstral, A.: The Airborne Snow Observatory: Fusion of scanning lidar, imaging spectrometer, and physically-based modeling for mapping snow water equivalent and snow albedo, Remote Sens. Environ., 184, 139–152, https://doi.org/10.1016/j.rse.2016.06.018, 2016.

Sun, S. and Xue, Y.: Implementing a new snow scheme in Simplified Simple Biosphere Model, Adv. Atmospheric Sci., 18, 335–354, https://doi.org/10.1007/BF02919314, 2001.